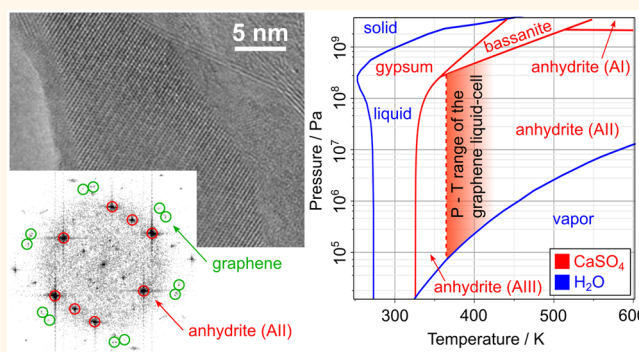


In Situ Crystallization of the Insoluble Anhydrite AII Phase in Graphene Pockets

Tibor Lehnert,[†] Michael K. Kinyanjui,[†] Anita Ladenburger,[†] Dimitri Rommel,[‡] Katharina Wörle,[‡] Felix Börrnert,[†] Kerstin Leopold,[‡] and Ute Kaiser^{*,†}

[†]Materialwissenschaftliche Elektronenmikroskopie and [‡]Institut für Analytische und Bioanalytische Chemie, Universität Ulm, Albert-Einstein-Allee 11, 89081 Ulm, Germany

ABSTRACT: Single-distilled water encapsulated in graphene pockets has been studied by aberration-corrected high-resolution transmission electron microscopy and electron energy loss spectroscopy at an acceleration voltage of 80 kV. Inside the graphene pockets, crystallization and *in situ* crystal growth are reported and identified as the insoluble AII phase of CaSO_4 (anhydrite) in a quasi-two-dimensional system. Its formation condition is discussed with respect to the possible temperature and van der Waals pressure between the graphene sheets.



KEYWORDS: graphene pocket, anhydrite, aberration-corrected HRTEM, encapsulated liquid, crystallization

Liquid cells allow the study of samples in a liquid environment in a transmission electron microscope (TEM),¹ as they serve as an enclosed system that isolates the liquids from the high-vacuum environment in the TEM of typically around 10⁻⁵ Pa and should add only low contrast to the recorded image.² Most experiments of liquid cells in TEM report the *in situ* observation of various processes in a liquid environment, such as growth of nanoparticles or electrochemical reactions or study of biological samples.¹⁻³

One of the challenges is to make liquid cells thin enough and ensure electron transparency and to undercut the mean free path of the electrons in the sample, thus enabling TEM investigations at high resolution. This applies to the cell window material as well as to the liquid itself. Other challenges include overcoming the image blur due to inelastic scattered electrons in combination with chromatic aberrations and due to electron beam-liquid interactions.² Recent developments allow the construction of nanostructured liquid cells with electron transparent windows made of thin SiN membranes fabricated on silicon microchips,^{4,5} thin carbon films,^{6,7} as well as from single-layer graphene.⁸

If a liquid is encapsulated between two single layers of graphene, van der Waals attraction forces can form and push the encapsulated material into narrow and closed graphene pockets, which in fact can be regarded as liquid cells.^{9,10} Typical bonding energies arising from van der Waals forces between the layers are in the range of 13–21 meV/Å², which were calculated for different layered materials including transition metal dichalcogenides, graphite, and boron nitride.¹¹ Moreover, the adhesion of graphene layers was also experimentally studied

with a blister test. For single-layer graphene, an adhesion energy of 45 meV/Å² was reported, and for two to five layers, the energy was 31 meV/Å².¹²

As one of the first applications, graphene liquid cells were used to investigate colloidal platinum nanocrystal growth with high-resolution TEM (HRTEM) for visualization of coalescence and structural reshaping.¹³ The growth of Pt–Pd nanoparticles inside graphene oxide liquid cells was also studied by TEM, and it was found that the growth as a function of time follows a power law, which in turn agrees with the Lifshitz–Slyozov–Wagner mechanism when the growing process is limited by surface reactions.¹⁴ Other investigations are directed to CuSO_4 and $\text{Ca}(\text{OH})_2$ in water encapsulated in graphene pockets, which are converted to CuO and CaO, respectively, due to pressure and ionization effects.¹⁰

In order to understand the behavior of the liquid itself in confinement, molecular dynamics simulations on the behavior of water between graphene layers have been performed. It was shown that water becomes anisotropic depending on the distance between the graphene sheets.³ Furthermore, it was reported that water is solid-like at graphene distances lower than 7 Å and arranges in a hexagonal structure because of the confinement within the graphite walls, and that it becomes liquid-like and does not show any clear order for distances around 20 Å.³ Further publications are concerned with the

Received: April 11, 2017

Accepted: July 24, 2017

Published: July 24, 2017

dynamics of nanobubbles confined in graphene pockets and the gas transport between the nanobubbles.¹⁵ They observed Ostwald ripening, coalescence of the bubbles, and determined the internal pressure of the nanobubbles to be in the range from 140 to 400 MPa depending on the bubble size.¹⁵ Despite the reported research efforts with graphene liquid cells, a basic understanding of the liquid dynamics, interfacial behavior, pressure environment, beam–liquid interactions, and heat transport is still lacking.

Modern transmission electron microscopes allow imaging with single atom resolution even at lower acceleration voltages ranging from 80 down to 20 kV,^{16–18} enabling the study of materials with knock-on damage thresholds far below 80 kV. Other damage mechanisms include radiolysis, heating, charging, and chemical etching.^{19,20} It has been shown that encapsulating beam-sensitive samples between graphene helps to reduce radiation damage up to 3 orders of magnitude.^{21–23} The high resistance of graphene against radiation damage is predominantly due to its high mechanical strength and high electrical and thermal conductivity.^{24–26} Due to these properties, and its high stability when using primary electron energies of 80 keV and below in the TEM,²⁷ graphene is a promising material for encapsulation of liquids^{3,13–15} and radiation-sensitive materials.^{21–23}

In this paper, we report on the crystallization of CaSO_4 from an aqueous solution, namely, single-distilled water, encapsulated in graphene. CaSO_4 shows a complex phase diagram, and depending on pressure and temperature, different phases exist. Possible CaSO_4 phases include the hydrous gypsum ($\text{CaSO}_4 \cdot 2\text{H}_2\text{O}$), the hemihydrate ($\text{CaSO}_4 \cdot 0.5\text{H}_2\text{O}$), and the anhydrite phase (CaSO_4).^{28–31} Moreover, the anhydrite exists in several phases, such as the AIII phase ($\gamma\text{-CaSO}_4$) with a hexagonal structure, the orthorhombic AII phase, and the monoclinic, high-pressure AI phase.^{28,29} The transition of gypsum to $\gamma\text{-CaSO}_4$ takes place at temperatures around 42–60 °C at 10^5 Pa.^{28,29} Depending on the water vapor pressure, the dehydration of hemihydrate to the soluble $\gamma\text{-CaSO}_4$ and its transformation into the insoluble AII phase occurs at temperatures between 100 and 150 °C.²⁹ At around 10^5 Pa and above 1100 °C, the AII phase can transform into the AI phase.³⁰ Furthermore, two triple points for the calcium sulfate minerals were found: At 235 MPa and 80 °C, the triple point between gypsum, hemihydrate, and anhydrite is located, and the second triple point appears at 2.15 GPa and 250 °C between hemihydrate, anhydrite AII phase, and the high-pressure AI phase (see Figure 5 and the more detailed discussions below).²⁸

RESULTS AND DISCUSSION

Total reflection X-ray fluorescence spectroscopy (TXRF) was performed to analyze encapsulated single-distilled water. It should be mentioned that single distillation of tap water is not sufficient to completely remove highly abundant alkali and earth alkali cations as well as common anions, such as sulfates, nitrates, and carbonates. This is reflected by a resistivity of the distilled water of approximately 0.1 to 1 $\text{M}\Omega\text{-cm}$, whereas high-purity water obtained by multistage purification exhibits a resistivity of 18.2 $\text{M}\Omega\text{-cm}$. Accordingly, traces of Ca and S were found in a ratio of 1 to 1.5 in the applied distilled water present as calcium cations Ca^{2+} and sulfate anions SO_4^{2-} at a pH of approximately 6. Besides these two elements, signals for phosphorus (P), chlorine (Cl), and potassium (K) were obtained, which are typically present as phosphates, chlorides,

and potassium cations (cf. Table 1). For light elements with an atomic number smaller 13, TXRF detection is difficult or not

Table 1. Molar Ratios of Detected Elements Compared to Calcium Set as 1^a

element	amount of substances	relative standard deviation (%)
phosphorus	23	33
sulfur	1.5	128
chlorine	0.83	91
potassium	1.5	97
calcium	1	
titanium	0.17	83
iron	0.066	95
nickel	0.11	55
copper	0.075	39
zinc	0.15	38

^aMeasurements for light elements are imprecise, so that high relative standard deviations occur like in the case of sulfur (number of replicate measurements is 6).

even possible. This includes Na as well as N and C that occur in the form of nitrate or carbonate, respectively.

In Figure 1, we present two subsequent TEM images of the liquid encapsulated between two graphene layers, taken at an

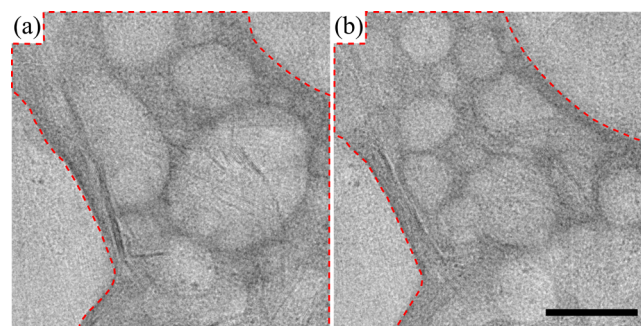


Figure 1. Images of 80 kV bright-field TEM showing water between two layers of graphene (a) and after 18 s in (b). The graphene pocket with the water is indicated with the dashed line. In the images, small bubbles (brighter areas) are surrounded by water (darker areas). The scale bar corresponds to 20 nm.

accelerating voltage of 80 kV. Because graphene is conductive, the graphene pocket is thin and not actively heated or cooled, so we assume room temperature in the TEM around the sample.^{20,32} Due to the interaction with the electron beam, the confined liquid (bubbles, brighter areas) moves within the graphene pocket. We observed growth and coalescence of the bubbles, which we interpret *via* the process known as Ostwald ripening.¹⁵ One important observation is that the encapsulated solution remains liquid despite the high-vacuum conditions in the microscope of 10^{-5} Pa. This is surprising because, at room temperature, water is liquid in a pressure range of kPa to MPa.³³ Thus, a graphene liquid cell must be characterized as an enclosed system with its own pressure environment originating from van der Waals forces between the two graphene sheets.^{9,10}

The van der Waals pressure for liquids between two single layers of graphene is reported as $P_{\text{vdW}} \approx E_{\text{AE}}/d$.³⁴ A value for the adhesion energy, E_{AE} , of a monolayer of graphene was experimentally determined to be 45 $\text{meV}/\text{\AA}^2$,¹² and the distance between two layers of graphene, d , is taken as ~ 3.4 \AA .²⁴ Then, the van der Waals pressure can increase to $P_{\text{vdW}} \approx 2$

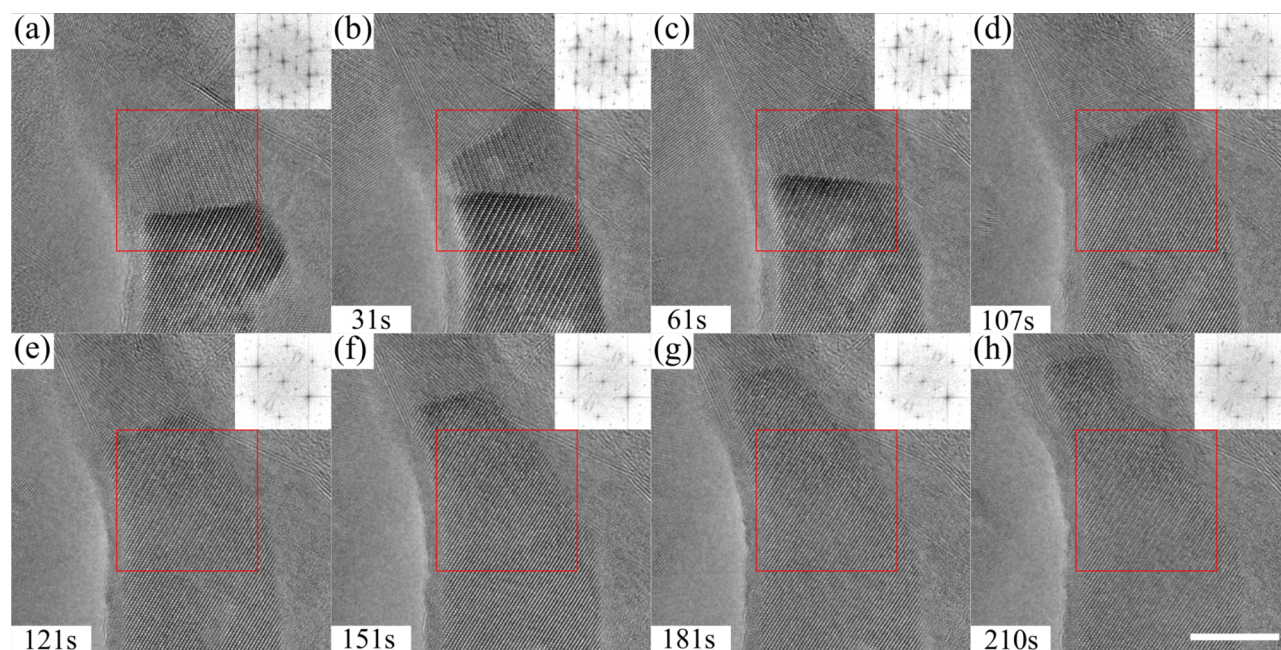


Figure 2. Series of 80 kV AC-HRTEM images showing the development of CaSO_4 crystals inside a graphene pocket under electron irradiation. (a) Initial image of CaSO_4 with two tilted crystalline $[100]$ orientations. The images (a–c) show a slow growing of the structure with the higher contrast at a rate of $\sim 0.70 \text{ nm}^2/\text{s}$. Fast Fourier transforms (FFTs) were made in the areas within the red frames. In the FFTs, one can clearly see the two tilted orientations with a tilt angle of about 43° . Image (d) shows that one orientation disappears by reorientation. The crystal adopts the orientation of the other CaSO_4 crystal. In the FFTs of the following images, it can be also seen that only one orientation is left (e–h). After the crystal orientation is adopted, the growth rate is increased to $\sim 1.05 \text{ nm}^2/\text{s}$. The white bar corresponds to 10 nm.

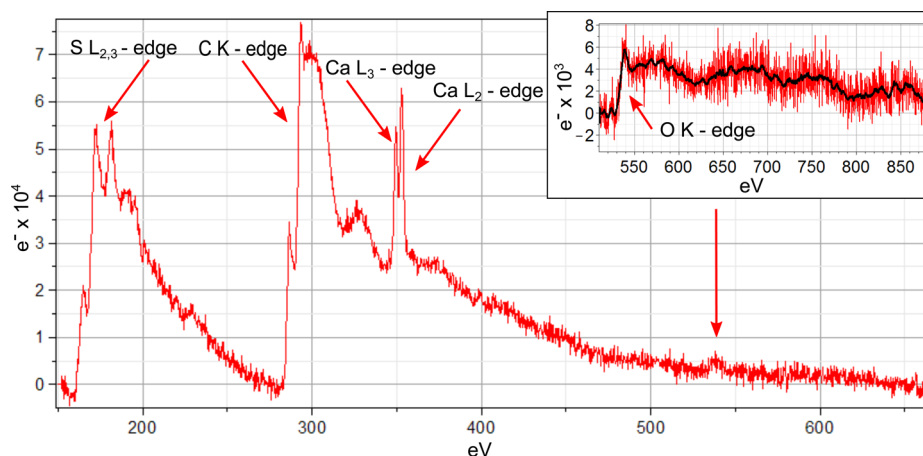


Figure 3. EELS data in the range of 150–650 eV of the CaSO_4 crystal. At 165 eV, the $L_{2,3}$ edge of sulfur; at 284 eV, the K edge of carbon; at 346 eV, the L_3 edge; and at 350 eV, the L_2 edge of calcium can be seen. The oxygen K peak at 532 eV is also visible. The O–K edge is shown in more detail in the inset. The black line shows the smoothed data of the recorded oxygen signal (red).

GPa. If we consider that water is in the liquid phase at distances of more than 20 \AA ,³ the van der Waals pressure exerted by a graphene pocket is approximately 360 MPa.

In Figure 2, we show an AC-HRTEM image sequence of a growing crystal from the aqueous solution (single-distilled water) obtained at 80 kV. In the images (a)–(c) a growth rate of about $0.7 \text{ nm}^2/\text{s}$ was measured. The growth rate in the images (e)–(h) increases to $\sim 1.05 \text{ nm}^2/\text{s}$. Before we further discuss the aberration-corrected (AC)-HRTEM data presented in Figure 2, we performed electron energy loss spectroscopy (EELS) experiments to identify the chemical nature of the crystals. As can be seen from the spectrum in Figure 3, calcium (Ca), sulfur (S), carbon (C), and oxygen (O) signals were found. The S– $L_{2,3}$ edge is located at 165 eV, and the Ca edge is

characterized by two peaks at 346 and 350 eV, which correspond to the L_3 and L_2 edges, respectively. The prominent peak at $\sim 284 \text{ eV}$ corresponds to the C–K edge, which occurs due to the graphene encapsulation of the solution. The O–K edge is located at 532 eV. In the inset, the O–K edge is shown in more detail, where the black line reflects the smoothed data of the oxygen peak. Furthermore, no additional peaks from other elements were found during the measurements on the crystal. The EELS data from the crystal confirm the existence of elements found also by TXRF measurements from the water solution.

With the knowledge of the EELS data and all known Ca, S, and O compounds, the images presented in Figure 2a–c are only conformed with an orthorhombic anhydrite crystal in the

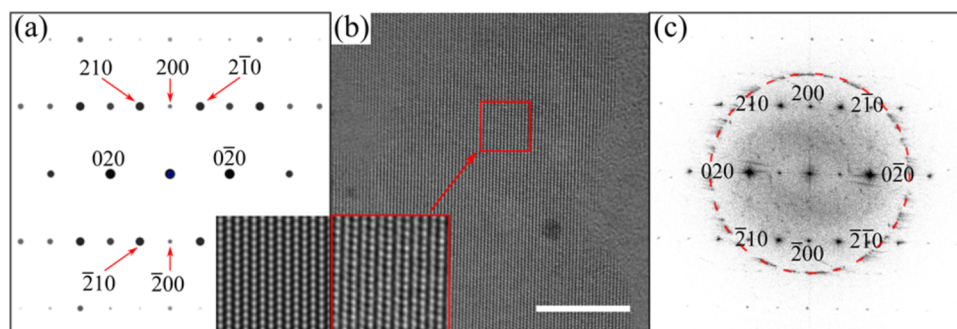


Figure 4. (a) Simulation of the diffraction pattern and HRTEM image of anhydrite CaSO_4 in the $[100]$ direction. Experimental recorded 80 kV AC-HRTEM image (b) where the inset shows a magnified area of the CaSO_4 . The scale bar corresponds to 10 nm. In the FFT (c) taken from (b), it can be clearly seen that an orthorhombic structure is present which corresponds to CaSO_4 in the $[100]$ direction. The two sets of reflections of the graphene layers are marked by the dashed ring (c).

$[100]$ projection. As can be seen, the simulated $[100]$ diffraction pattern and $[100]$ HRTEM image of CaSO_4 (crystal thickness of three unit cells (2.1 nm) was taken for the simulation) in the AII phase in Figure 4a do match the experimental AC-HRTEM in (b) and the fast Fourier transform (FFT) in (c) taken from (b) (cf. Table 2, where experimental

Table 2. Comparison between Measured Distances in the FFT and Simulated Diffraction Pattern of Anhydrite CaSO_4 ^a

reflections	experimental data (nm ⁻¹)	simulated data (nm ⁻¹)
(210)	3.51(3)	3.51
(200)	3.21(3)	3.21
(2 $\bar{1}$ 0)	3.49(3)	3.51
(020)	2.85(3)	2.86
(2 $\bar{1}$ 0)	3.51(3)	3.51
($\bar{2}$ 00)	3.18(3)	3.21
($\bar{2}$ 10)	3.49(3)	3.51
(020)	2.88(3)	2.86

^aThe experimental data are in good agreement with the simulated values. The number in the brackets gives the confidence interval of the last digits.

data and simulated data for anhydrite are listed; the agreement between the experimental and the simulated data is always within the given confidence interval of our measurement).

Moreover, we see in Figure 2 two CaSO_4 crystals which are tilted toward each other and this way hinder each other's growth and reduce the growth rate until the thicker area (higher contrast) reshapes the thinner part. After reshaping, one orientation disappears (Figure 2d), which could be caused by the attempt of the system to reduce its surface energy. Afterward, the growth rate increases by a factor of ~ 1.5 . In addition, the crystal grows in a sample area that seems to be contaminated. This area is slightly thicker than the left parts of images (a–h), which also explains the appearance of the bright edge across the images. The origin of the contamination is very likely hydrocarbons from the preparation of the sample in air or residues of the encapsulated water.

To summarize, Figure 2 shows that the crystallization of CaSO_4 is slowed down when the two $[100]$ crystals are in contact (within the red square in Figure 2a–c). Subsequently, an Ostwald ripening process starts—in agreement with the Lifshitz–Slyozov–Wagner theory, which conciliate the reduction of energy at the boundary. The smaller crystal then disappears and just one CaSO_4 crystal remains, which can be

also seen in the disappearing reflections in the FFTs in Figure 2d–h.

Lateral crystal sizes of CaSO_4 in the AII phase were found to be on the order of $\sim 10^3 \text{ nm}^2$. Due to the small thickness of the graphene pocket, the encapsulated anhydrite was treated as a quasi-two-dimensional crystal. However, to get a profound understanding, we performed thickness-dependent $[100]$ HRTEM image simulation of one (0.7 nm), two (1.4 nm), and three unit cells (2.1 nm), as seen in Figure 5a. In Figure 5c, the line scans from the simulations in (a) and the experiment in (b) are compared. We can see the best agreement with a thickness of two unit cells. However, fluctuations in contrast of the single atom columns are clearly seen. Thus, we assume a crystal thickness between two and three unit cells.

The crystallization of the quasi-two-dimensional anhydrite phase from the liquid is a surprising result because, in a standard 3D system, it crystallizes only at high pressures and high temperatures.²⁸ We are now going to discuss this phase transformation in light of our nanoscale experiment. We start with the macroscale p – T diagram of CaSO_4 .

The crystallization process of bulk anhydrite has been discussed in the literature.^{28–30} The CaSO_4 – H_2O systems are characterized by dehydration reactions in high-pressure ranges and at temperature ranges of 50–300 °C, which is given in a p – T phase diagram.²⁸ The triple point between gypsum, bassanite, and anhydrite was found to be at 235 MPa and 80.5 °C.²⁸ Figure 6 displays an overlay of p – T phase diagrams for water and CaSO_4 to give a classical view on the crystallization conditions; however, we have to be aware that the classical view on the nanoscale is not necessarily valid. Based on the p – T phase diagrams, one can estimate the pressure and temperature within the graphene liquid cell to be in the ranges of $\sim 100 \text{ kPa}$ to $\sim 230 \text{ MPa}$ and of 100–150 °C, respectively.

Interestingly, $\sim 230 \text{ MPa}$ is in the range of earlier published values for the pressure in graphene liquid cells.^{9,15} However, a temperature of 100–150 °C for the crystallization is not likely because direct heating due to the electron beam has been estimated to be minor in very thin materials²⁰ and the efficient heat dissipation of graphene,²⁵ as mentioned above.

In earlier studies, the effect of temperature for transformations on the nanoscale is not unambiguously detectable.³² Furthermore, it was reported that the melting temperature of nanoparticles is much lower than that of their bulk counterparts.^{35,36} This was predicted by theoretical calculations and confirmed by experimental data showing that the solid–liquid transition temperature decreases with smaller nanocrystal

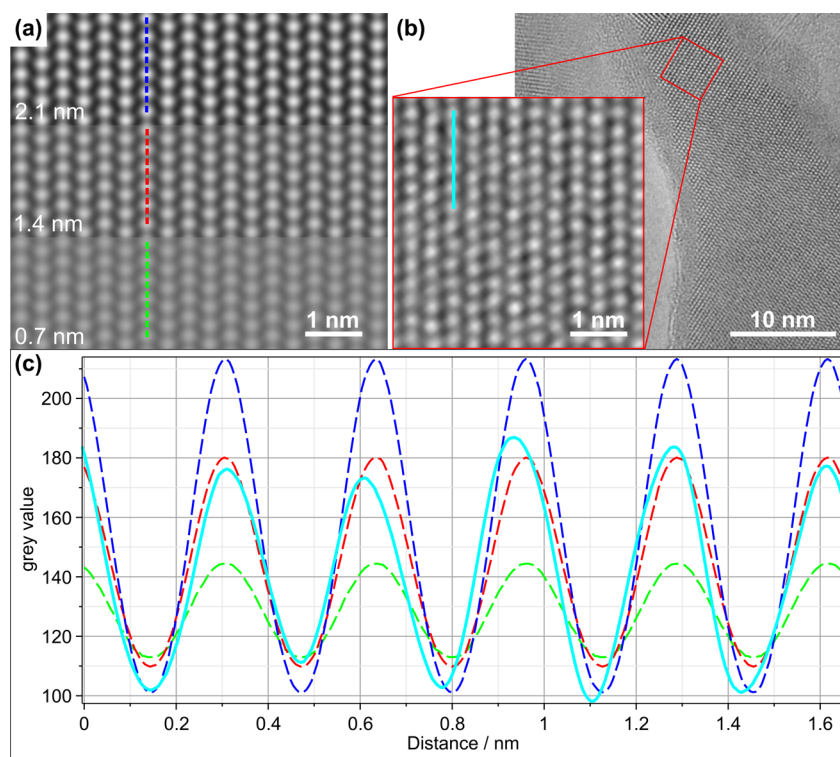


Figure 5. (a) [001] HRTEM simulations of anhydrite dependent on the thicknesses [0.7 nm (1 unit cell), 1.4 nm (2 unit cells), 2.1 nm (3 unit cells)]. (b) Experimental HRTEM image magnified from the red square in the overview image. Line scans in (c) were taken from the dashed and solid lines in (a) and (b), respectively. The contrast comparison shows good agreement for two unit cell thick crystals (1.4 nm).

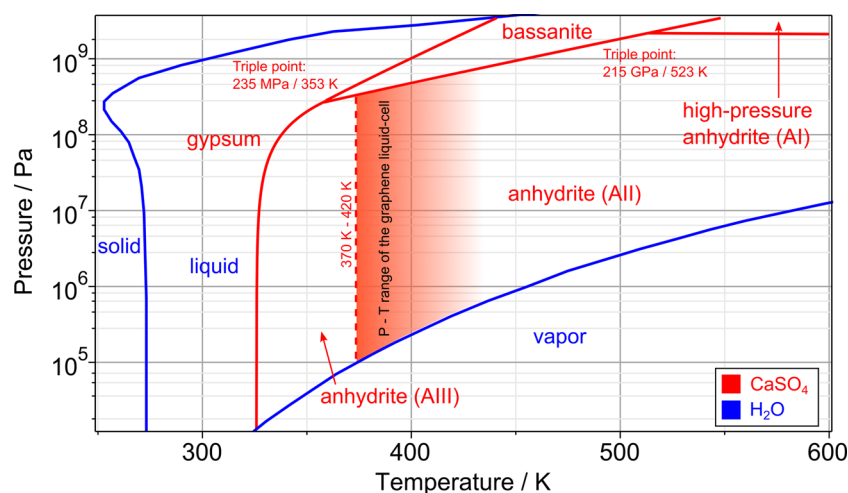


Figure 6. Overlay of the phase diagrams for CaSO₄ (red)²⁸ and H₂O (blue).³³ The pressure and temperature range, where the crystallization in bulk material takes place, is marked with the color gradient. The probability that the temperature is much higher than 370–420 K is low because of the graphene encapsulation which increases the heat conduction so that a certain amount of the excessive thermal energy can be disposed.

size.^{35,36} Here, we are now going to estimate the thickness-dependent change of the transition temperature in thin CaSO₄ films from a very simple model. We determine the surface-to-volume ratio as a function of the thickness, D , of the nanofilm, with $T_n = T_0(1 - 3r/D)$.^{37,38} T_n is the transition temperature of the nanofilm, T_0 is the transition temperature of the corresponding bulk material, and r is the minimal possible thickness of the material. In Figure 7, T_n is plotted over the thickness D of the anhydrite film. The different curves, red and blue, correspond to transition temperatures T_0 in the bulk at 150 and 100 °C, respectively. For a thickness of 1.4 nm, T_0 is in

the range of 24–37 °C, and for 2.1 nm, it is in the range of 50–74 °C. Thus, the estimation of the reduced temperature for a 2.1 nm thin anhydrite agrees both with our understanding of a nearly room temperature experiment in a graphene pocket and with our estimation of the thickness from the comparison of the contrast between image simulation and experiment (cf. Figure 5).

CONCLUSIONS

In conclusion, we reported on the crystallization inside graphene pockets out of single-distilled water, which contained

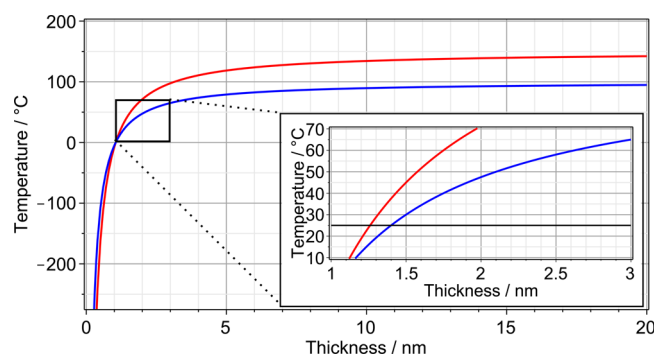


Figure 7. Theoretical determined behavior of the transition temperature of anhydrite from nano- to macroscale. The two different lines, red and blue, arise due to the range of transition temperatures in bulk at a macroscale of 150 and 100 °C, respectively. From the inset, it can be seen that the transition temperature decreases to room temperature (25 °C, black line) at crystal thicknesses of about 1.25 to 1.40 nm.

Ca and S as main trace components. By AC-HRTEM and EELS experiments, we found that quasi-two-dimensional CaSO_4 crystals in the insoluble anhydrite AII phase had been formed, which was confirmed by HRTEM image simulations. Their formation conditions were discussed with the help of the macroscale p – T phase diagram of CaSO_4 , considering the van der Waals pressure inside the graphene pockets and the reduction of the crystallization temperature in an experiment on the nanoscale.

METHODS

Single-distilled water has been analyzed by TXRF measurements using a high-efficiency S2 Picofox spectrometer (Bruker Nano GmbH, Germany). The incident X-ray beam is produced by an air-cooled low-power Mo X-ray tube operated at 50 kV and 600 μA . Detection was carried out perpendicular to the quartz glass sample carrier by a silicon drift detector with an area of 30 mm^2 . Controlling the apparatus and spectra deconvolution was performed by Spectra 7 software (version 7.2.5.0, Bruker Nano GmbH). Ten microliters of the distilled water sample was transferred onto the precleaned and blank-tested sample carrier and heated to 70 °C for controlled evaporation of water. Three individual sample carriers were prepared analogously for statistical evaluation, and each was measured twice with a live time of 500 s. Element ratios (setting Ca to 1) were calculated after Bayesian deconvolution from signal intensities, taking into account element-specific sensitivity.

Two grids with chemical vapor deposited graphene grown on a copper substrate were prepared. A few TEM grids were placed on the surface of the graphene-covered copper, together with a drop of isopropyl alcohol ($\text{C}_3\text{H}_8\text{O}$). The evaporation of the $\text{C}_3\text{H}_8\text{O}$ resulted in the grids adhering to the surface of the graphene-covered copper substrate. In the next step, the copper was then etched away with a 0.35 M ammonium peroxodisulfate (APS) solution, so that the grids with the graphene remain on the APS solution. They were fished out with a sieve and cleaned with water. From this, a sandwich with water pockets was produced by taking the first grid with a tweezer and putting a drop of 2 μL of single-distilled water on the graphene-covered side. The second grid was placed on top, with the graphene facing the first grid. During the drying process, the grids came into contact and encapsulated the remaining water in the pockets.

A third-order spherical aberration-corrected FEI Titan 80-300 was used for imaging in HRTEM mode with an acceleration voltage of 80 kV. The experiment was performed with dark atom contrast, $C_s \approx 20 \mu\text{m}$ and an extraction voltage of 2000 V. The images were acquired with dose rates on the order of $10^6 \text{ e}/(\text{nm}^2 \text{ s})$ and a vacuum level of

10^{-5} Pa. It is assumed that the specimen and the sample holder are at near-ambient temperature.

AUTHOR INFORMATION

Corresponding Author

*E-mail: ute.kaiser@uni-ulm.de.

ORCID

Tibor Lehnert: [0000-0002-4904-9580](https://orcid.org/0000-0002-4904-9580)

Notes

The authors declare no competing financial interest.

ACKNOWLEDGMENTS

The authors acknowledge financial support by the DFG in the framework of the “SALVE” (Sub Angstrom Low-Voltage Electron microscopy) project as well the Ministry of Science, Research and the Arts (MWK) of Baden-Wuerttemberg in the framework of the SALVE project.

REFERENCES

- (1) Liao, H.-G.; Zheng, H. Liquid Cell Transmission Electron Microscopy. *Annu. Rev. Phys. Chem.* **2016**, *67*, 719–47.
- (2) De Jonge, N.; Ross, F. M. Electron Microscopy of Specimens in Liquid. *Nat. Nanotechnol.* **2011**, *6*, 695–704.
- (3) Mosaddeghi, H.; Alavi, S.; Kowsari, M. H.; Najafi, B. Simulations of Structural and Dynamic Anisotropy in Nano-Confined Water Between Parallel Graphite Plates. *J. Chem. Phys.* **2012**, *137*, 184703.
- (4) Williamson, M. J.; Tromp, R. M.; Vereecken, P. M.; Hull, R.; Ross, F. M. Dynamic Microscopy of Nanoscale Cluster Growth at the Solid-Liquid Interface. *Nat. Mater.* **2003**, *2*, 532–536.
- (5) Grogan, J. M.; Bau, H. H. The Nanoaquarium: A Platform for *In Situ* Transmission Electron Microscopy in Liquid Media. *J. Microelectromech. Syst.* **2010**, *19*, 885–894.
- (6) Nishijima, K.; Yamasaki, J.; Orihara, H.; Tanaka, N. Development of Microcapsules for Electron Microscopy and their Application to Dynamical Observation of Liquid Crystals in Transmission Electron Microscopy. *Nanotechnology* **2004**, *15*, S329–S332.
- (7) Daulton, T. L.; Little, B. J.; Lowe, K.; Jones-Meehan, J. *In Situ* Environmental Cell-Transmission Electron Microscopy Study of Microbial Reduction of Chromium(VI) Using Electron Energy Loss Spectroscopy. *Microsc. Microanal.* **2001**, *7*, 470–485.
- (8) Mohanty, N.; Fahrenholtz, M.; Nagaraja, A.; Boyle, D.; Berry, V. Impermeable Graphenic Encasement of Bacteria. *Nano Lett.* **2011**, *11*, 1270–1275.
- (9) Khestanova, E.; Guinea, F.; Fumagalli, L.; Geim, A. K.; Grigorieva, I. V. Universal Shape and Pressure inside Bubbles Appearing in Van der Waals Heterostructures. *Nat. Commun.* **2016**, *7*, 12587.
- (10) Vasu, K. S.; Prestat, E.; Abraham, J.; Dix, J.; Kashtiban, R. J.; Beheshtian, J.; Sloan, J.; Carbone, P.; Neek-Amal, M.; Haigh, S. J.; Geim, A. K.; Nair, R. R. Van der Waals Pressure and its Effect on Trapped Interlayer Molecules. *Nat. Commun.* **2016**, *7*, 12168.
- (11) Björkman, T.; Gulans, A.; Krashenninnikov, A. V.; Nieminen, R. M. Van der Waals Bonding in Layered Compounds from Advanced Density-Functional First Principles Calculations. *Phys. Rev. Lett.* **2012**, *108*, 235502.
- (12) Koenig, S. P.; Boddeti, N. G.; Dunn, M. L.; Bunch, J. S. Ultrastrong Adhesion of Graphene Membranes. *Nat. Nanotechnol.* **2011**, *6*, 543–546.
- (13) Yuk, J. M.; Park, J.; Ercius, P.; Kim, K.; Hellebusch, D. J.; Crommie, M. F.; Lee, J. Y.; Zettl, A.; Alivisatos, A. P. High-Resolution EM of Colloidal Nanocrystal Growth Using Graphene Liquid Cells. *Science* **2012**, *336*, 61–64.
- (14) De Clercq, A.; Dachraoui, W.; Margeat, O.; Pelzer, K.; Henry, C. R.; Giorgio, S. Growth of Pt-Pd Nanoparticles Studied *In Situ* by HRTEM in a Liquid Cell. *J. Phys. Chem. Lett.* **2014**, *5*, 2126–2130.

- (15) Shin, D.; Park, J. B.; Kim, Y. J.; Kim, S. J.; Kang, J. H.; Lee, B.; Cho, S. P.; Hong, B. H.; Novoselov, K. S. Growth Dynamics and Gas Transport Mechanism of Nanobubbles in Graphene Liquid Cells. *Nat. Commun.* **2015**, *6*, 6068.
- (16) Kaiser, U.; Biskupek, J.; Meyer, J.; Leschner, J.; Lechner, L.; Rose, H.; Stöger-Pollach, M.; Khlobystov, A.; Hartel, P.; Müller, H.; Haider, M.; Eyhusen, S.; Benner, S. Transmission Electron Microscopy at 20kV for Imaging and Spectroscopy. *Ultramicroscopy* **2011**, *111* (8), 1239–1246.
- (17) Suenaga, K.; Sato, Y.; Liu, Z.; Kataura, H.; Okazaki, T.; Kimoto, K.; Sawada, H.; Sasaki, T.; Omoto, K.; Tomita, T.; Kaneyama, T.; Kondo, Y. Visualizing and Identifying Single Atoms Using Electron Energy-Loss Spectroscopy with Low Accelerating Voltage. *Nat. Chem.* **2009**, *1*, 415–418.
- (18) Linck, M.; Hartel, P.; Uhlemann, S.; Kahl, F.; Müller, H.; Zach, J.; Haider, M.; Niestadt, M.; Bischoff, M.; Biskupek, J.; Lee, Z.; Lehnert, T.; Börrnert, F.; Rose, H.; Kaiser, U. Chromatic Aberration Correction for Atomic Resolution TEM Imaging from 20 to 80 k. *Phys. Rev. Lett.* **2016**, *117*, 076101.
- (19) Egerton, R. Control of Radiation Damage in the TEM. *Ultramicroscopy* **2013**, *127*, 100.
- (20) Egerton, R.; Li, P.; Malac, M. Radiation Damage in the TEM and SEM. *Micron* **2004**, *35*, 399.
- (21) Algara-Siller, G.; Kurasch, S.; Sedighi, M.; Lehtinen, O.; Kaiser, U. The Pristine Atomic Structure of MoS₂ Monolayer Protected from Electron Radiation Damage by Graphene. *Appl. Phys. Lett.* **2013**, *103* (20), 203107.
- (22) Zan, R.; Ramasse, Q. M.; Jalil, R.; Georgiou, T.; Bangert, U.; Novoselov, K. S. Control of Radiation Damage in MoS₂ by Graphene Encapsulation. *ACS Nano* **2013**, *7* (11), 10167–10174.
- (23) Lehnert, T.; Lehtinen, O.; Algara-Siller, G.; Kaiser, U. Electron Radiation Damage Mechanisms in 2D MoSe₂. *Appl. Phys. Lett.* **2017**, *110* (3), 033106.
- (24) Castro Neto, A. H.; Guinea, F.; Peres, N. M. R.; Novoselov, K. S.; Geim, A. K. The Electronic Properties of Graphene. *Rev. Mod. Phys.* **2009**, *81* (1), 109.
- (25) Balandin, A. A.; Ghosh, S.; Bao, W.; Calizo, I.; Teweldebrhan, D.; Miao, F.; Lau, C. N. Superior Thermal Conductivity of Single-Layer Graphene. *Nano Lett.* **2008**, *8*, 902–907.
- (26) Lee, C.; Wei, X.; Kysar, J. W.; Hone, J. Measurement of the Elastic Properties and Intrinsic Strength of Monolayer Graphene. *Science* **2008**, *321*, 385–388.
- (27) Meyer, J. C.; Eder, F.; Kurasch, S.; Skakalova, V.; Kotakoski, J.; Park, H.-J.; Roth, S.; Chuvilin, A.; Eyhusen, S.; Benner, G.; Krashenninnikov, A. V.; Kaiser, U. Accurate Measurement of Electron Beam Induced Displacement Cross Sections for Single-Layer Graphene. *Phys. Rev. Lett.* **2012**, *108*, 196102.
- (28) Mirwald, P. W. Experimental Study of the Dehydration Reactions Gypsum-Bassanite and Bassanite-Anhydrite at High Pressure: Indication of Anomalous Behavior of H₂O at High Pressure in the Temperature Range of 50–300 °C. *J. Chem. Phys.* **2008**, *128*, 074502.
- (29) Freyer, D.; Voigt, W. Crystallization and Phase Stability of CaSO₄ and CaSO₄-Based Salts. *Monatsh. Chem.* **2003**, *134*, 693–719.
- (30) Liu, C.; Zheng, H.; Du, J.; Wang, D. The Effect of Pressure on the Kinetics of γ -Anhydrite Crystallization Investigated by Diamond Anvil Cell. *J. Cryst. Growth* **2015**, *410*, 39–46.
- (31) Morales, J.; Astilleros, J. M.; Fernández-Díaz, L. Nanoscopic Characteristics of Anhydrite (100) Growth. *Cryst. Growth Des.* **2012**, *12*, 414–421.
- (32) Börner, P.; Kaiser, U.; Lehtinen, O. Evidence Against a Universal Electron-Beam-Induced Virtual Temperature in Graphene. *Phys. Rev. B: Condens. Matter Mater. Phys.* **2016**, *93*, 134104.
- (33) Atkins, P.; De Paula, J. *Atkins' Physical Chemistry*; Oxford University Press, 2010.
- (34) Algara-Siller, G.; Lehtinen, O.; Wang, F. C.; Nair, R. R.; Kaiser, U.; Wu, H. A.; Geim, A. K.; Grigorieva, I. V. Square Ice in Graphene Nanocapillaries. *Nature* **2015**, *519*, 443–445.
- (35) Li, H.; Han, P. D.; Zhang, X. B.; Li, M. Size-Dependent Melting Point of Nanoparticles Based on Bond Number Calculation. *Mater. Chem. Phys.* **2013**, *137*, 1007–1011.
- (36) Jiang, H.; Moon, K.; Dong, H.; Hua, F.; Wong, C. P. Size-Dependent Melting Properties of Tin Nanoparticles. *Chem. Phys. Lett.* **2006**, *429*, 492–496.
- (37) Xie, D.; Wang, M. P.; Qi, W. H. A Simplified Model to Calculate the Surface-to-Volume Atomic Ratio Dependent Cohesive Energy of Nanocrystals. *J. Phys.: Condens. Matter* **2004**, *16*, L401–L405.
- (38) Mirjalili, M.; Vahdati-Khaki, J. Prediction of Nanoparticles' Size-Dependent Melting Temperature Using Mean Coordination Number Concept. *J. Phys. Chem. Solids* **2008**, *69*, 2116–2123.